Photonic density of states of two-dimensional quasicrystalline photonic structures

Lin Jia, Ion Bita,* and Edwin L. Thomas†

Institute for Soldier Nanotechnologies, Department of Materials Science and Engineering, Massachusetts Institute of Technology, Cambridge, Massachusetts 02139

(Received 28 April 2011; published 18 August 2011)

A large photonic band gap (PBG) is highly favorable for photonic crystal devices. One of the most important goals of PBG materials research is identifying structural design strategies for maximizing the gap size. We provide a comprehensive analysis of the PBG properties of two-dimensional (2D) quasicrystals (QCs), where rotational symmetry, dielectric fill factor, and structural morphology were varied systematically in order to identify correlations between structure and PBG width at a given dielectric contrast (13:1, Si:air). The transverse electric (TE) and transverse magnetic (TM) PBGs of 12 types of QCs are investigated (588 structures). We discovered a 12*mm* QC with a 56.5% TE PBG, the largest reported TE PBG for an aperiodic crystal to date. We also report here a QC morphology comprising "throwing star"-like dielectric domains, with near-circular air cores and interconnecting veins emanating radially around the core. This interesting morphology leads to a complete PBG of ∼20% , which is the largest reported complete PBG for aperiodic crystals.

DOI: 10.1103/PhysRevA.84.023831 PACS number(s): 42.70.Qs, 61.44.Br, 78.67.Pt

Photonic crystals (PCs), invented in 1987 [1], have abilities to control the flow of light [2–15] primarily because of their photonic band gap (PBG) properties [16,17]. Two-dimensional (2D) photonic quasicrystals (PQCs) have been shown to be promising PBG materials because of their nearly isotropic photonic band structures stemming from their high rotational symmetries [18,19], defect-free localized modes [20–22], and the possibility to open a PBG at a lower refractive index contrast than typical PC structures [23,24]. PQCs have attracted additional interest for a variety of photonic applications, including lensing [25], waveguiding [26,27], negative refraction [28], and optical fiber devices [29].

An essential requirement for many applications of PBG materials is the gap size. The first study of PQC structures was published in 1998 and focused on 8*mm* symmetric quaiscrystals (QCs) [30]. At a dielectric contrast of 10:1, Chan found a transverse magnetic (TM) gap of 22% for structures consisting of isolated dielectric rods, while a corresponding 8*mm* vein-connected dielectric structure displayed a 25% transverse electric (TE) gap and no complete PBGs [30]. In 2000, a published report on the properties of 12-fold rotationally symmetric QCs suggested that even higher rotational symmetries could lead to significant improvements over conventional photonic crystals, and claimed finding a complete PBG of 30% at an astoundingly low dielectric contrast of only 4:1 [31]. Soon after, the results of this paper were contradicted; structures with air rods decorating the vertices of a 12*mm* square-triangular tiling exhibited only a modest complete PBG that opens at a dielectric contrast >7:1 [32]. Many theoretical investigations of QC PBG properties ensued, including Penrose structures [33], 5*mm* QCs [18], 8*mm* QCs [23,34], and various 12*mm* QCs [32,35]. A list of the various QC structures and the associated PBG properties and corresponding dielectric contrasts is presented in supplementary material [36]. However, due to the various differences in the focus and material assumptions in these studies, it is quite difficult to conduct a direct comparison and detailed structure-property analysis to identify design elements for optimizing the PBG properties of 2D QCs of different symmetries and morphologies. For example, the impact of morphology on the size of TM PBG has been somewhat obscured, though recently the strong influence of the resonance of discrete dielectric features has been identified in independent studies [33,37–41]. While the importance of large PBG sizes for applications of PBG material-based devices has been well recognized, in the case of QC much work remains to be done towards identifying the champion QC structures, with the largest TM, TE, and complete PBGs.

In this report, we conduct a comprehensive study of the impact of rotational symmetry and morphology on the PBGs of 12 different types of 588 QCs, assuming the constitutive materials are silicon and air ($\varepsilon_2 : \varepsilon_1 = 13 : 1$). The QCs investigated are defined by level set equations [42,43] that can be fabricated by interference lithography [44–48], and QCs generated by decorating quasiperiodic geometric tilings according to a particular recipe [49,50], which can be fabricated via e-beam lithography or focused ion beam lithography. We examined both TE and TM PBGs, for 8*mm*, 10*mm*, and 12*mm* rotational symmetries, for a very wide dielectric fill ratio range (0.02–0.98), and both structural morphologies (dielectric-filled, or air-filled). For each QC type in this extensive set of morphologies and symmetries, we used finite-difference time-domain (FDTD) simulations to find the optimum filling ratio that maximizes the TM or the TE PBG. Champion QCs with the largest TM, the largest TE, and the largest complete PBG are discussed and analyzed and the physical origins of the gaps are described.

The first family of 2D QCs investigated is generated using the following level set equation:

$$f(x,y) = \sum_{n=0}^{N-1} \cos[2\pi x \cos(\pi n/N)/a + 2\pi y \sin(\pi n/N)/a]. \quad (1)$$

*Present address: Qualcomm MEMS Technologies, San Jose, CA 95134.

†Corresponding author: elt@mit.edu

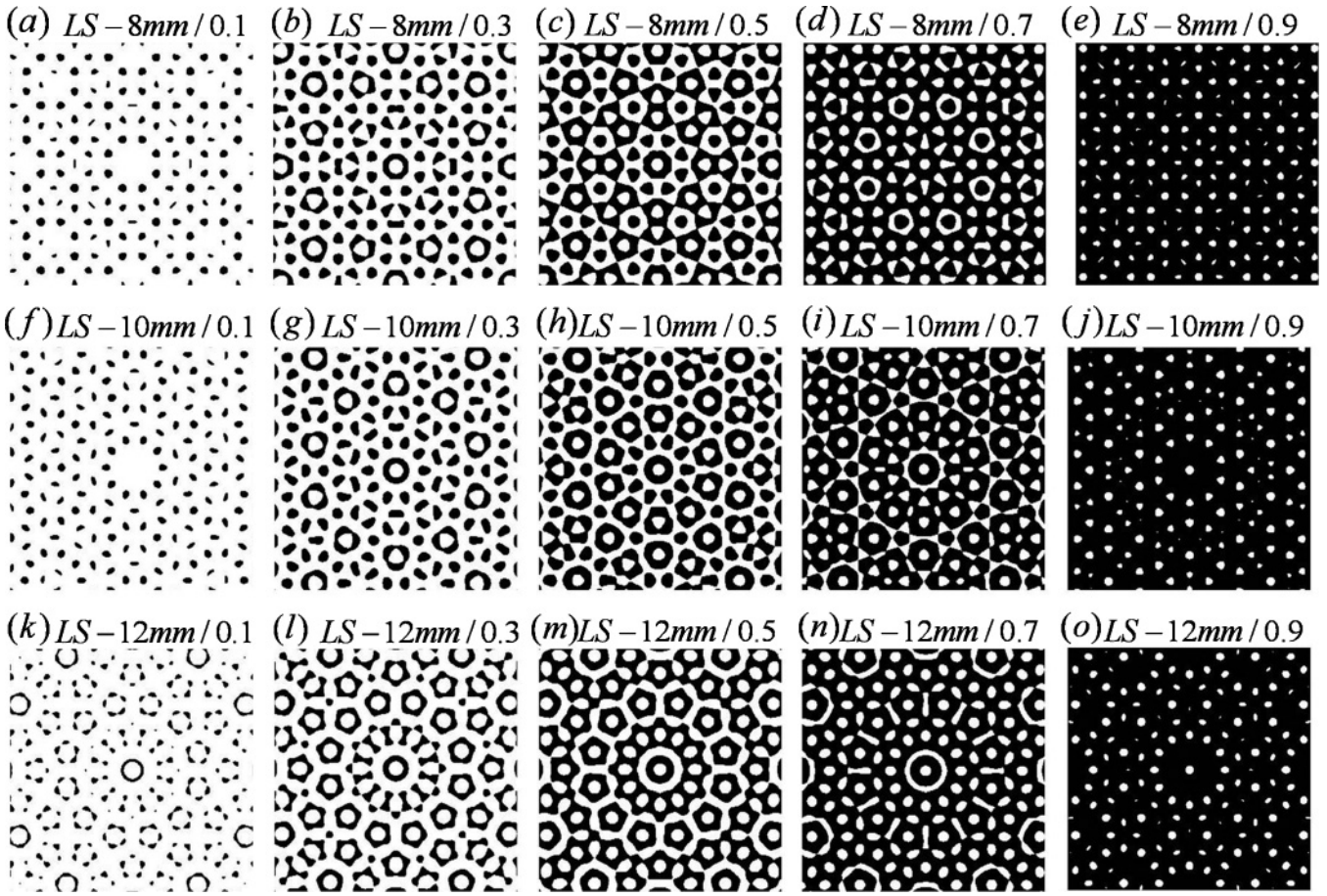

FIG. 1. (a)–(e) Structural evolution with fill factor for 8*mm* symmetric QCs defined by level set equation (1). Here the last number behind LS − 8*mm*/ is the filling ratio of the black component. For a negative photoresist, a black component indicates the dielectric; for a positive photoresist, the black color indicates air features in a dielectric surrounding; (f)–(j) Structural evolution with fill factor for 10*mm* symmetric QCs defined by level set equation (1); (k)–(o): structural evolution with fill factor for 12*mm* symmetric QCs defined by level set equation (1).

The value of $2N$ in Eq. (1) sets the rotational symmetry of the associated QCs, and a represents the characteristic unit length. QCs defined by level set equation (1) can be fabricated by multiple-exposure interference lithography (MEIL) [44,51,52]. Equation (1) can be used to generate two types of QC structure morphologies, using an analogy with the photoresist tone in MEIL: (i) positive tone, where the dielectric material of choice is found at all locations where $f(x,y) < t$ (air fills the rest of the space), and (ii) negative tone, where the dielectric material occupies all locations where $f(x,y) > t$. Since large rotational symmetries involve increasing fabrication difficulties due to a reduced structural contrast associated with increasing the number of exposures, we focused our studies on QCs with $N < 7$. For $N = 1,2,3$, the structures are periodic. For $N = 4,5,6$, the structures are quasiperiodic with rotational symmetries 8*mm*, 10*mm*, and 12*mm*, respectively. Some representative QC morphologies from this study are shown in Fig. 1. The rotation center of MEIL is assumed to be at the high light intensity position of the one-dimensional (1D) periodic fringe pattern, which generates additional mirror symmetries. The resultant highest point group symmetries for eightfold, tenfold, and twelvefold QCs are 8*mm*, 10*mm*, and 12*mm*. Here we use LS-8*mm*, LS-10*mm*, and LS-12*mm* to denote 8*mm*, 10*mm*, and 12*mm* QCs generated from level set equation (1).

The second set of QC structures studied is generated by decorating quasiperiodic geometric tilings obtained by 2D projection from a higher dimensional space [49,50]. Here, we consider the approach of placing rods (dielectric or air) at the nodes of the chosen tilings, and filling the region between the rods with the complementary material (dielectric rods in air, or vice versa for the opposite structural morphology). Representative QCs of various symmetries are shown in Fig. 2. We use RQC (or ARQC) to denote QCs generated from placing dielectric (or air) rods at the nodes of the chosen tilings.

The PBG of these 2D QC structures can be determined from maps of the local density of states (LDOS) [23,34,53–55] calculated using a FDTD solution to Maxwell's equations [56,57]. In a LDOS map, a continuous low-LDOS region along the vertical frequency axis indicates a PBG. We first discuss the results for TM polarized waves in QCs defined by the level set equation (1). The LDOS maps for the 8*mm*, 10*mm*, and 12*mm* QCs are shown in Fig. 3. As the filling ratio of the structures (f) is varied from 0.02 to 0.98, a number of regions with gaps are found. For the negative tone LS-8*mm* QC shown in Fig. 3(a), the largest TM PBG size is 37.0% , occurring at $f = 0.18$.

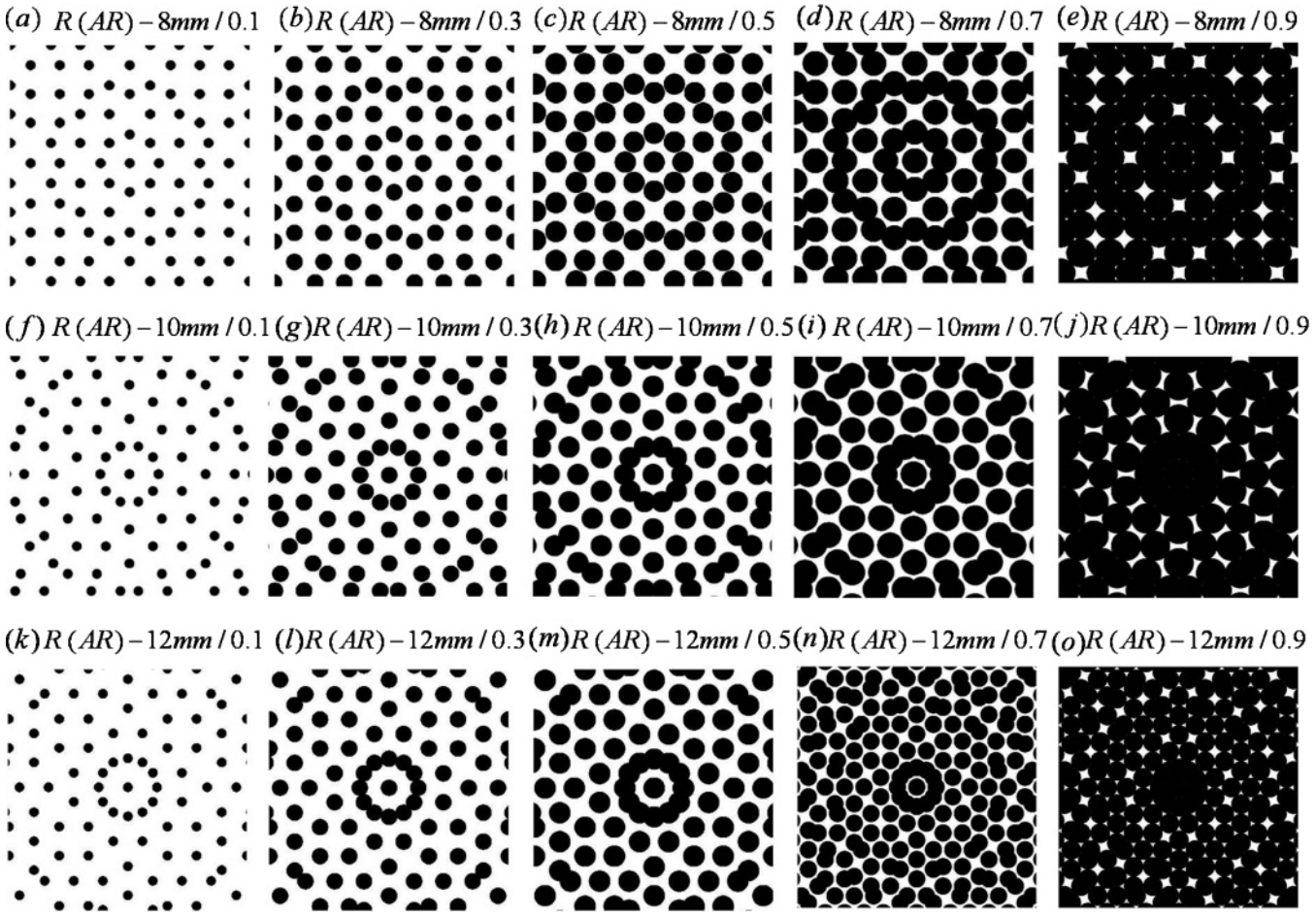

FIG. 2. (a)–(e) QCs of 8*mm* rotational symmetry from quasiperiodic tiling patterns decorated with rods. Here the number after R − 8*mm*/ is the filling ratio of the black component; (f)–(j) QCs of 10*mm* rotational symmetry from quasiperiodic tiling patterns decorated with rods; (k)–(o) QCs of 12*mm* rotational symmetry from quasiperiodic tiling patterns decorated with rods. For RQCs, the black color indicates the dielectric and the white color indicates the air, whereas for ARQCs, the black color indicates the air and the white color indicates the dielectric.

For the positive tone LS-8*mm* QC shown in Fig. 3(b), a similar sized TM PBG also occurs at $f = 0.18$. For the negative tone LS-10*mm* QC shown in Fig. 3(c), an interesting observation is that the lowest TM PBG width remains almost constant for a wide range of filling fractions and this insensitivity makes it a good candidate for experimental photonic devices. For the positive tone LS-10*mm* QC shown in Fig. 3(d), the largest TM PBG size is 37.2% at $f = 0.12$. For the negative tone LS-12*mm* QC shown in Fig. 3(e), the largest TM PBG size is 40.7% for $f = 0.14$. For the positive tone LS-12*mm* QC shown in Fig. 3(f), a large TM PBG of ∼42% appears in the range of $0.1 \leqslant f \leqslant 0.2$, implying another excellent candidate for photonic devices. The comprehensive results of this study are collected in Table I.

Next we analyze the TM PBGs of QCs defined by placing solid rods (R-) or air rods (AR-) of desired diameter at the vertices of various QC geometric tilings obtained from hyperspace projection. Interestingly, for R-8*mm*, R-10*mm*, and R-12*mm* QCs, as well as the reference case of a triangular lattice PC (R-p6*mm*), the TM LDOS gaps are all found to be quite similar; see Figs. 4(a)–4(d). The similarity of the LDOS for these structures in the region with $f < 0.25$ is due to the dominant role of the Mie resonances generated by individual dielectric rods [38,39,41]. Although the rotational symmetries of the QCs are different, the identity of the individual scatterer is preserved and is found to lead to similar PBG properties for the various quasiperiodic arrangements we investigated. At larger fill fractions the averaged edge-edge distance of the rods becomes small and the TM PBG closes quickly, which can be associated with a loss of distinct Mie resonances in the case of interconnected dielectric domains. The largest observed TM PBGs of R-p6*mm*, R-8*mm*, R-10*mm*, and R-12*mm* QCs are listed in Table I. The largest PBGs (>45%) occur at $f = 0.12$ for the dielectric contrast of 13:1 used in this study. Compared to TM PBGs of RQCs, ARQCs are found to display smaller TM PBGs, as shown in Table I and Fig. 5.

In order to better understand why RQCs have superior TM gap properties compared to ARQCs and LSQCs, we examine their corresponding structural characteristics. It is known that morphologies consisting of separate dielectric domains can have a large TM PBG, thus we start with exploring the impact of the dielectric domain shapes and arrangements. Based on our calculations shown in Table I and from the data in Ref. [18], QCs consisting of entirely circular-shaped features, e.g., rods on the nodes of quasiperiodic tilings, have

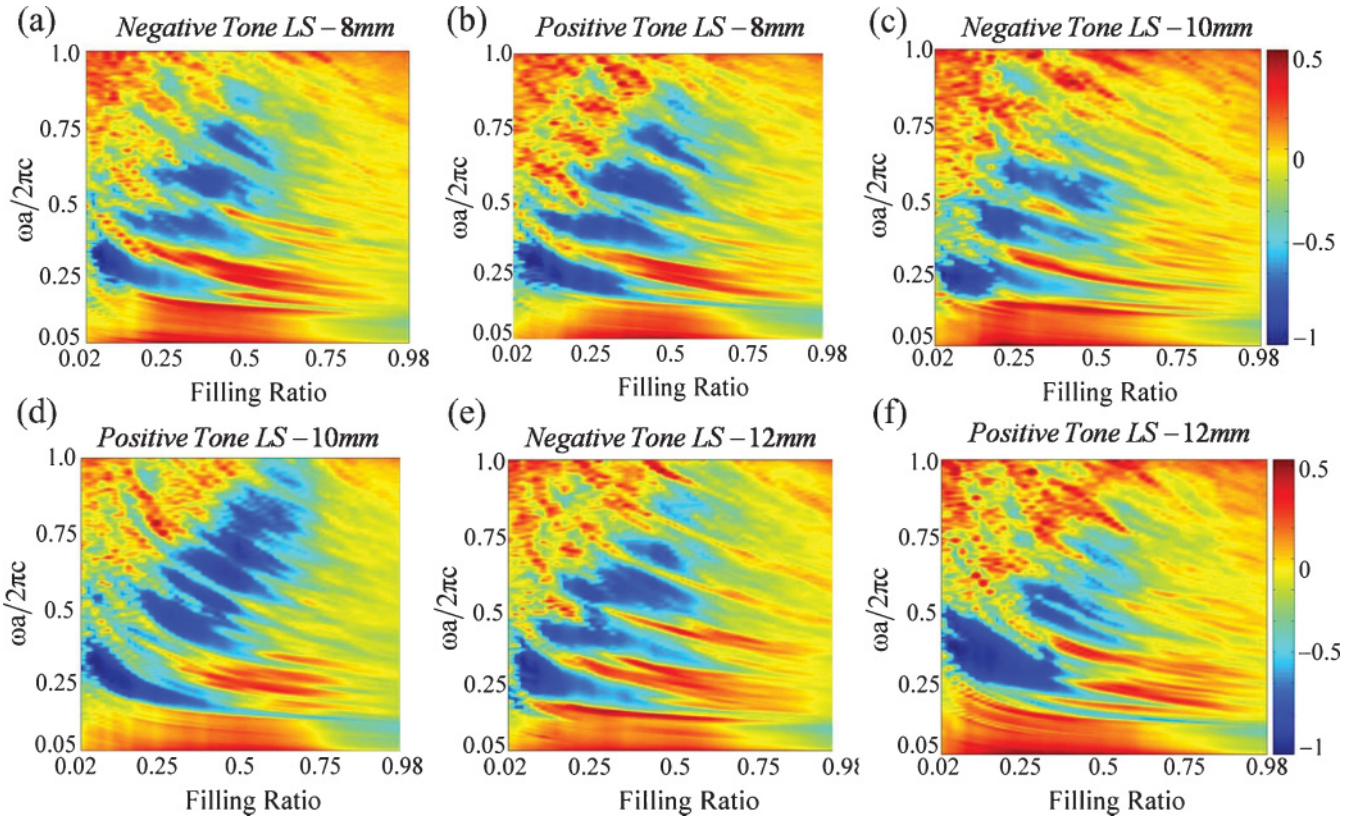

FIG. 3. (Color online) (a)–(f) TM photonic LDOS maps for LS-8*mm*, LS-10*mm*, and LS-12*mm* QCs, with log (LDOS) plotted vs fill ratio and frequency.

the best TM PBG properties. Further, the TM PBGs of QCs consisting of separated noncircular features (one group of level set equation: LS-8*mm*, LS-10*mm*, and LS-12*mm*) are smaller than the TM PBGs of QCs consisting of near-circular

TABLE I. Summary of key findings from the LDOS numerical calculations. The results are for $\varepsilon_2/\varepsilon_1 = 13:1$. Here f is the optimal filling ratio for large PBG.

Quasicrystal type	Mode	f	$\omega_{\text{lower}}a/2\pi c$	$\omega_{\text{upper}}a/2\pi c$	$\omega_{\text{middle}}a/2\pi c$	$\Delta\omega/\omega_{\text{center}}$
Negative tone LS-8*mm*	TM	0.18	0.22	0.32	0.27	37.0%
Positive tone LS-8*mm*	TM	0.18	0.22	0.32	0.27	37.0%
Negative tone LS-10*mm*	TM	0.24−0.38	∼0.21	∼0.28	∼0.245	∼28.5%
Positive tone LS-10*mm*	TM	0.12	0.235	0.3425	0.289	37.2%
Negative tone LS-12*mm*	TM	0.14	0.225	0.34	0.2825	40.7%
Positive tone LS-12*mm*	TM	0.1−0.2	∼0.285	∼0.447	∼0.366	∼44%
R-8*mm*	TM	0.12	0.292	0.472	0.382	47.1%
R-10*mm*	TM	0.12	0.280	0.448	0.364	46.1%
R-12*mm*	TM	0.12	0.294	0.470	0.382	46.0%
AR-8*mm*	TM	0.08	0.225	0.295	0.26	26.9%
AR-10*mm*	TM	0.1	0.26	0.325	0.2925	22.6%
AR-12*mm*	TM	0.16	0.417	0.51	0.4635	21.2%
AR-12*mm*	TE	0.32	0.26	0.465	0.362	56.5%
AR-12*mm*	Complete	0.18	0.41	0.5	0.455	19.8%
R-p6*mm* (crystal)	TM	0.12	0.297	0.493	0.395	49.6%
R-p6*mm* (crystal)	TE	0.44	0.292	0.336	0.314	13.77%
R-p6*mm* (crystal)	Complete	Any	0	0	0	0
Honeycomb (crystal)	TE	0.22	0.225	0.47	0.3475	59.3%
Honeycomb (crystal)	TM	Any	0	0	0	0
AR-p6*mm* (crystal)	TE	0.36	0.252	0.424	0.338	50.9%
AR-p6*mm* (crystal)	TM	0.1	0.483	0.585	0.534	19.1%
AR-p6*mm* (crystal)	Complete	0.18	0.413	0.497	0.455	18.5%

features (five to ten groups of level set equation, shown in Ref. [18]). A noncircular element has different scattering cross sections for waves incident from different angles, which is disadvantageous for wave propagation suppression for all in-plane directions. For example, the separated dielectric features of ARQCs with a low filling ratio, as shown in Figs. 2(e), 2(j), and 2(o), are star shaped or a rectangular shape with sharp corners. Such features are strongly anisotropic scatterers; therefore their TM PBGs are small, as can be seen in Table I and Fig. 5. Furthermore, besides the importance of optimizing the shape of the individual dielectric domain, it is important to emphasize the importance of their spatial arrangement. R-p6*mm* PC structures display larger TM PBG than the corresponding RQCs, benefiting from added coherent Bragg scattering. In RQC structures, the larger variation of nearest-neighbor distances further limits the resonance optimization.

We now proceed to examine the results for the TE LDOS calculations. In general, TE PBGs are favored for a structure comprised of a network of connected veins. For example, the honeycomb vein structure is the champion photonic crystal structure with the largest TE PBG of 60% for $\varepsilon_1/\varepsilon_2 = 13.0$ [58]. As shown in the supplementary material [59], the TE PBGs of all the QC structures examined in this study are found to be much smaller (<10%), with one notable exception. In the case of the AR-12*mm* QC structure, we found a very large TE PBG of 56.5% at $f = 0.32$, which is the largest TE PBG observed to date for QCs and only slightly lower than the champion honeycomb structure [60]. The PBG gap map of AR-12*mm* QC and the LDOS plot for the champion AR-12*mm* QC are shown in Figs. 6(c) and 6(d) and the corresponding AR-12*mm* morphology at $f = 0.32$ is shown in Fig. 6(a). The high rotational symmetry leads to high density of interconnected veins. To identify some correlations between structure and TE PBG properties, we also examine the case of the periodic honeycomb crystal (AR-p6*mm*) for which we compute the LDOS map and analyze the underlying morphology. Interestingly, we find a very similar TE gap range, as shown in Table I, and, furthermore, many common structural motifs between the AR-12*mm* QC structure and the AR-p6*mm* PC structure, shown in Figs. 6(a) and 6(b). The primary difference between the honeycomb structure and AR-12*mm* QC is that the nodes connecting the veins of the AR-12*mm* QC all contain a small round central dielectric core feature. We believe that the repeating motifs of the "throwing star"-like dielectric domains, with near-circular cores and interconnecting veins emanating radially, are key for simultaneously enabling complete gaps (overlapping TE and TM gaps), as discussed in this paper.

To display a large complete PBG, the photonic structure needs to enable TM and TE gaps that are both large and have overlapping frequency intervals. The complete PBGs of most of the QCs examined in the present work are minimal (i.e., <10%). AR-12*mm* is the only exception with a TM PBG and a TE PBG >20% , as shown in Table I. At $f = 0.18$, the AR-12*mm* QC has the largest complete PBG (19.8%), which is essentially the same as the largest complete PBG found to date (20.1%) [61] and it is the largest reported value for aperiodic crystals. A portion of the champion AR-12*mm* QC is shown in more detail in Fig. 6(e). Comparing the AR-12*mm* QC in Fig. 6(a) ($f = 0.32$) and the same structure with a lower filling ratio in Fig. 6(e) ($f = 0.18$), we find that as we decrease the filling ratio, the dielectric veins become thinner compared to the dielectric core, causing the TE PBG to shrink rapidly from 56.5% to 20% while the TM PBG increases from 0% to ∼20%. The physical reason for this

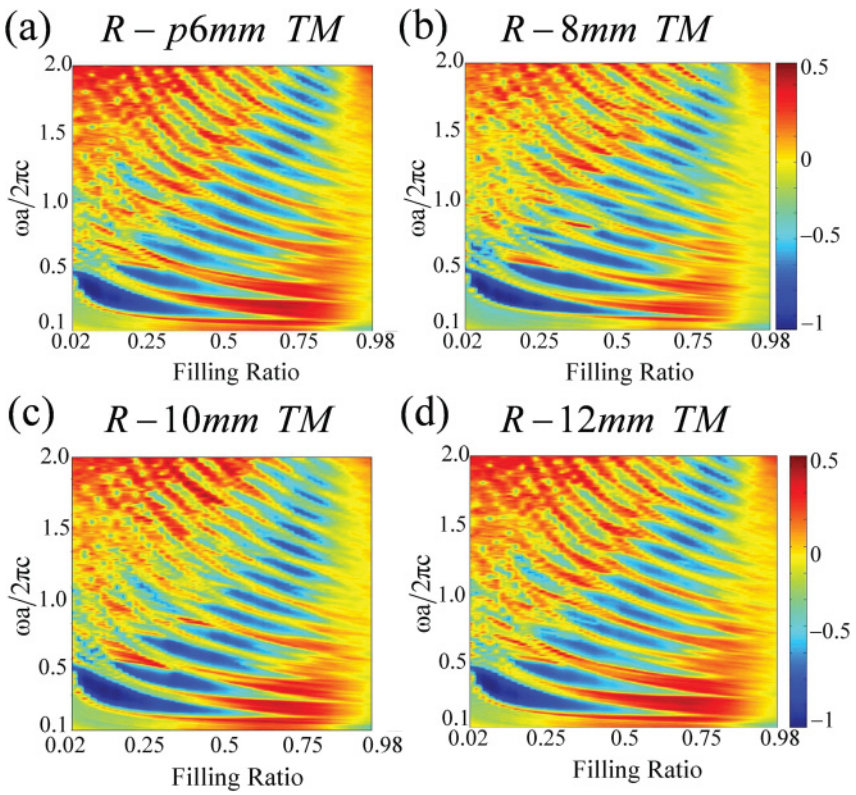

FIG. 4. (Color online) (a)–(d) TM photonic LDOS maps for periodic R-p6*mm* and the quasiperiodic R-8*mm*, R-10*mm*, and R-12*mm* QCs, with log (LDOS) plotted vs fill ratio and frequency.

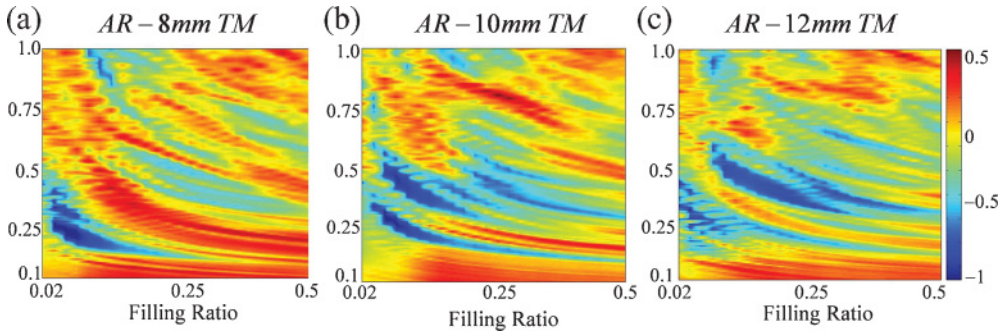

FIG. 5. (Color online) (a)–(c) TM photonic LDOS maps for AR-8*mm*, AR-10*mm*, and AR-12*mm* QCs, with log (LDOS) plotted vs fill ratio and frequency. The ARQCs with a low filling ratio have a wide range of shapes and sizes of the discrete dielectric regimes [see Figs. 2(e), 2(j), and 2(o)] and they provide relatively weak TM gaps.

behavior is that the veins contribute to the TE PBG through a destructive Bragg interference mechanism. As the vein thickness decreases, the strength of destructive interference decreases and the TE PBG shrinks. For thinner veins, their corresponding connection points consist of a relatively larger dielectric portion of the total and act as effective "particles", as shown in Fig. 6(e). The resonant scattering of these "particles" enables the formation of the TM PBG. Therefore the large, complete PBG of the AR-12*mm* at $f = 0.18$ is enabled by its morphology comprising simultaneously a thin dielectric vein network, which contributes a large TE PBG, and the set of "throwing star"-like dielectric particles, which contributes a large TM PBG. If the filling ratio is further decreased, e.g., to 0.12, the veins are broken and the QC is no longer self-connected, leaving isolated square-shape dielectric particles—not surprisingly, in this case the corresponding TE PBG is zero while the TM PBG is still ∼20%.

In conclusion, we computed and analyzed in detail the LDOS of two families of 2D photonic QCs, generated from level set equations and from quasiperiodic tiling patterns decorated with rods, for three different rotational symmetries (8, 10, and 12). We found that (1) for QCs comprising individual dielectric features, TM PBGs are largely impacted by the feature shape and feature interdistance. QCs consisting of dielectric rods with uniform diameter, as produced by decorating quasiperiodic tiling patterns, exhibit better TM PBGs than QCs consisting of noncircular features, as typically obtained in structures produced from level set equations.

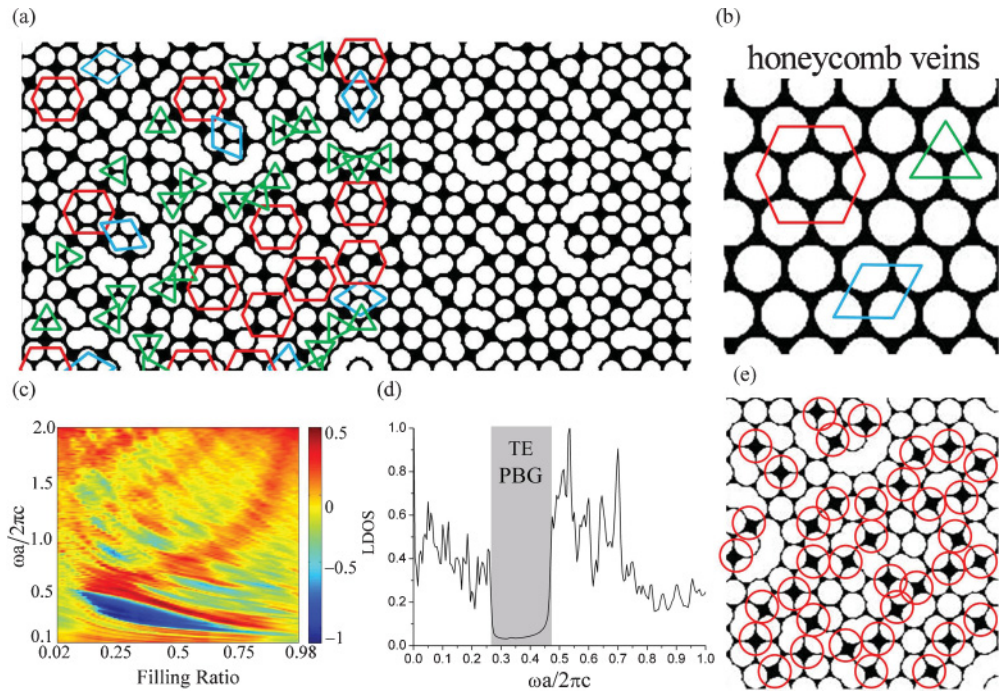

FIG. 6. (Color online) (a) The champion AR-12*mm* structure with the largest TE PBG (56.5%). The filling ratio of the structure is 0.32; (b) schematic delineating the periodic honeycomb veins (AR-p6*mm*): honeycomb, rhombus, and triangles; (c) TE photonic LDOS maps for AR-12*mm* QCs, with log (LDOS) plotted vs fill ratio and frequency; (d) the LDOS plot for the champion structure ($f = 0.32$); the TE PBG is indicated in the figure; (e) the champion AR-12*mm* QC with the largest complete PBG at $f = 0.18$. The "throwing star"-like dielectric resonator particles are indicated in the circles. This RV (resonator-vein) structure exhibits good short-range order.

(2) R-8*mm*, R-10*mm*, and R-12*mm* QCs are found to exhibit large TM PBGs (>45%), close to the TM PBG of the current champion structure (∼50% for the R-p6*mm*), supporting the conclusion that their PBG properties are dominated by Mie resonances of the individual dielectric domains, with only a small impact from the particular rotational symmetry. (3) The TE PBGs of QCs investigated here are found to be very small (10%), except for the case of the AR-12*mm* QC where we find a very large TE PBG (56.5% at $f = 0.32$), which is only slightly lower than the champion TE PBG size (the honeycomb structure has a TE PBG ∼60% for $\varepsilon_1/\varepsilon_2 = 13.0$ at $f = 0.22$). As shown in Figs. 6(a) and 6(b), the AR-12*mm* structure has a large number of structural motifs of honeycomb veins, which are associated with the large TE PBG observed; (4) the AR-12*mm* QC is also found to have a large, complete PBG (19.8%) at $f = 0.18$. In this case, the corresponding morphology consists of "throwing star"-like dielectric domain motifs, with an "effective" particle in the center and interconnected veins radiating around the particle core, enabling formation of both TE and TM gaps; (5) the DOS maps provide detailed information about PBG properties obtained from different QC morphology design choices (symmetry, dielectric shapes, filling ratios, and structure morphology). The optimized QCs which have the largest PBGs are listed in Table I, which enables direct comparison of the PBG properties of this large set of QCs, and provides useful guidance for further photonic QC device design and optimization.

ACKNOWLEDGMENTS

This research is supported by the US Army Research Office through the Institute for Soldier Nanotechnologies, under Contract No. W911NF-07-D-0004 and by NSF, under Grant No. DMR-0804449. The authors thank Dr. Mihai Ibanescu for providing an implementation of the projection algorithm for generating quasiperiodic lattices, and for useful discussions.

[1] E. Yablonovitch, Phys. Rev. Lett. **58**, 2059 (1987).
[2] A. Blanco *et al.*, Nature **405**, 437 (2000).
[3] M. Makarova *et al.*, Appl. Phys. Lett. **92**, 161107 (2008).
[4] A. Gopinath *et al.*, Nano Lett. **8**, 2423 (2008).
[5] S. Y. Lin *et al.*, Science **282**, 274 (1998).
[6] Z. Yu, G. Veronis, Z. Wang, and S. Fan, Phys. Rev. Lett. **100**, 023902 (2008).
[7] M. L. Povinelli *et al.*, Appl. Phys. Lett. **84**, 3639 (2004).
[8] M. L. Povinelli, S. G. Johnson, and J. D. Joannopoulos, Opt. Express **13**, 7145 (2005).
[9] Y. Akahane *et al.*, Nature **425**, 944 (2003).
[10] M. L. Povinelli and S. H. Fan, Appl. Phys. Lett. **89**, 191114 (2006).
[11] Y. Fink *et al.*, Science **282**, 1679 (1998).
[12] L. Dal Negro *et al.*, Appl. Phys. Lett. **84**, 5186 (2004).
[13] S. H. Fan, P. R. Villeneuve, J. D. Joannopoulos, and E. F. Schubert, Phys. Rev. Lett. **78**, 3294 (1997).
[14] B. H. Cumpston *et al.*, Nature **398**, 51 (1999).
[15] M. F. Yanik and S. Fan, Phys. Rev. Lett. **92**, 083901 (2004).
[16] M. Maldovan and E. L. Thomas, Nat. Mater. **3**, 593 (2004).
[17] C. K. Ullal *et al.*, Appl. Phys. Lett. **84**, 5434 (2004).
[18] M. C. Rechtsman *et al.*, Phys. Rev. Lett. **101**, 073902 (2008).
[19] M. Florescu, S. Torquato, and P. J. Steinhardt, Phys. Rev. B **80**, 155112 (2009).
[20] K. Mnaymneh and R. C. Gauthier, Opt. Express **15**, 5089 (2007).
[21] R. C. Gauthier and K. Mnaymneh, Opt. Commun. **264**, 78 (2006).
[22] A. Della Villa *et al.*, Opt. Express **14**, 10021 (2006).
[23] J. L. Yin *et al.*, Opt. Commun. **269**, 385 (2007).
[24] G. Zito *et al.*, Microwave Optical Technol. Lett. **51**, 2732 (2009).
[25] E. Di Gennaro, C. Miletto, S. Savo, A. Andreone, D. Morello, V. Galdi, G. Castaldi, and V. Pierro, Phys. Rev. B **77**, 193104 (2008).
[26] C. J. Jin *et al.*, Appl. Phys. Lett. **75**, 1848 (1999).
[27] H. H. Tao *et al.*, J. Vac. Sci. Technol. B **25**, 1609 (2007).
[28] X. H. Deng *et al.*, J. Mod. Opt. **57**, 325 (2010).
[29] S. Kim and C. S. Kee, Opt. Express **17**, 15885 (2009).
[30] Y. S. Chan, C. T. Chan, and Z. Y. Liu, Phys. Rev. Lett. **80**, 956 (1998).
[31] M. E. Zoorob *et al.*, Nature **404**, 740 (2000).
[32] X. Zhang, Z. Q. Zhang, and C. T. Chan, Phys. Rev. B **63**, 081105 (2001).
[33] A. Della Villa, S. Enoch, G. Tayeb, V. Pierro, V. Galdi, and F. Capolino, Phys. Rev. Lett. **94**, 183903 (2005).
[34] G. Zito *et al.*, J. Opt. A: Pure Appl. Opt. **11**, 024007 (2009).
[35] R. C. Gauthier and K. Mnaymneh, Opt. Express **13**, 1985 (2005).
[36] See Supplemental Material at http://link.aps.org/supplemental/10.1103/PhysRevA.84.023831 for the information in supplementary Table I.
[37] C. Rockstuhl, U. Peschel, and F. Lederer, Opt. Lett. **31**, 1741 (2006).
[38] E. Lidorikis and M. M. Sidalas, Phys. Rev. B **61**, 13458 (2000).
[39] C. Rockstuhl and F. Lederer, New J. Phys. **8**, 206 (2006).
[40] L. N. Shi, X. Y. Jiang, and C. F. Li, J. Phys.: Condens. Matter **19**, 176214 (2007).
[41] R. L. Chern and S. D. Chao, Opt. Express **16**, 16600 (2008).
[42] C. K. Ullal *et al.*, J. Opt. Soc. Am. A **20**, 948 (2003).
[43] A. Avgeropoulos *et al.*, Macromolecules **30**, 5634 (1997).
[44] I. Bita *et al.*, Adv. Mater. **19**, 1403 (2007).
[45] J. B. Yeo *et al.*, J. Vac. Sci. Technol. B **27**, 1886 (2009).
[46] X. Wang *et al.*, Appl. Phys. Lett. **88**, 051901 (2006).
[47] W. Y. Tam, Appl. Phys. Lett. **89**, 251111 (2006).
[48] J. Xu *et al.*, Opt. Express **15**, 4287 (2007).
[49] D. Levine and P. J. Steinhardt, Phys. Rev. Lett. **53**, 2477 (1984).
[50] M. Senechal, *Quasicrystals and Geometry* (Cambridge University Press, Cambridge, UK, 1996).
[51] N. D. Lai *et al.*, Opt. Express **14**, 10746 (2006).
[52] R. C. Gauthier and A. Ivanov, Opt. Express **12**, 990 (2004).
[53] K. Busch and S. John, Phys. Rev. E **58**, 3896 (1998).
[54] V. I. Kopp *et al.*, Opt. Lett. **23**, 1707 (1998).
[55] S. Y. Zhu, Y. Yang, H. Chen, H. Zheng, and M. S. Zubairy, Phys. Rev. Lett. **84**, 2136 (2000).

[56] L. Jia and E. L. Thomas, J. Opt. Soc. Am. B **26**, 1882 (2009).
[57] W. S. Kim, L. Jia, and E. L. Thomas, Adv. Mater. **21**, 1921 (2009).
[58] M. Florescu, S. Torquato, and P. J. Steinhardt, Appl. Phys. Lett. **97**, 201103 (2010).
[59] See Supplemental Material at http://link.aps.org/supplemental/10.1103/PhysRevA.84.023831 for the information in supplementary Figs. 1 and 2.
[60] O. Sigmund and K. Hougaard, Phys. Rev. Lett. **100**, 153904 (2008).
[61] L. F. Shen, Z. Ye, and S. He, Phys. Rev. B **68**, 035109 (2003).